



UNIVERSITY OF LEEDS

This is a repository copy of *A case-study of cold-air pool evolution in hilly terrain using field measurements from COLPEX*.

White Rose Research Online URL for this paper:
<http://eprints.whiterose.ac.uk/142347/>

Version: Accepted Version

Article:

Jemmett-Smith, BC, Ross, AN orcid.org/0000-0002-8631-3512, Sheridan, PF et al. (2 more authors) (2019) A case-study of cold-air pool evolution in hilly terrain using field measurements from COLPEX. *Quarterly Journal of the Royal Meteorological Society*, 145 (720). pp. 1290-1306. ISSN 0035-9009

<https://doi.org/10.1002/qj.3499>

© 2019 Crown copyright. *Quarterly Journal of the Royal Meteorological Society* © 2019 Royal Meteorological Society. This is the peer reviewed version of the following article: Jemmett-Smith, BC, Ross, AN, Sheridan, PF, Hughes, JK, Vosper, SB. A case-study of cold-air pool evolution in hilly terrain using field measurements from COLPEX. *Q J R Meteorol Soc.* 2019; 145: 1290– 1306, which has been published in final form at <https://doi.org/10.1002/qj.3499>. This article may be used for non-commercial purposes in accordance with Wiley Terms and Conditions for Self-Archiving. Uploaded in accordance with the publisher's self-archiving policy.

Reuse

Items deposited in White Rose Research Online are protected by copyright, with all rights reserved unless indicated otherwise. They may be downloaded and/or printed for private study, or other acts as permitted by national copyright laws. The publisher or other rights holders may allow further reproduction and re-use of the full text version. This is indicated by the licence information on the White Rose Research Online record for the item.

Takedown

If you consider content in White Rose Research Online to be in breach of UK law, please notify us by emailing eprints@whiterose.ac.uk including the URL of the record and the reason for the withdrawal request.



eprints@whiterose.ac.uk
<https://eprints.whiterose.ac.uk/>

A case study of cold air pool evolution in hilly terrain using field measurements from COLPEX

Bradley C. Jemmett-Smith¹ | Andrew N. Ross¹ | Peter F. Sheridan² | John K. Hughes¹ | Simon B. Vosper²

¹School of Earth and Environment,
University of Leeds, Leeds, UK

²Met Office, Exeter, UK

Correspondence

Andrew N. Ross, School of Earth and Environment, University of Leeds, Leeds, LS2 9JT, UK
Email: A.N.Ross@leeds.ac.uk

Funding information

NERC CASE studentship with the UK Met Office. NERC / UK Met Office Joint Weather and Climate Research Programme grant NE/I007679/1. The National Centre for Atmospheric Science (NCAS) provide financial support for the deployment of the lidar and AWS.

A case study investigation of cold air pool (CAP) evolution in hilly terrain is conducted using field measurements made during IOP 16 of the COLd air Pool EXperiment (COLPEX). COLPEX was designed to study cold air pooling in small scale valleys typical of the UK (~100-200 m deep, ~1 km wide). The synoptic conditions during IOP 16 are typical of those required for CAPs to form during the night, with high pressure, clear skies and low ambient winds. Initially a CAP forms around sunset and grows uninterrupted for several hours. However, starting 4 h after sunset a number of interruptions to this steady cooling rate occur. Three episodes are highlighted from the observations and the cause of disruption attributed to; (1) wave activity, in the form of gravity waves and/or Kelvin-Helmholtz (KH) instability, (2) increases in the above-valley winds resulting from the development of a nocturnal low level jet (NLLJ), (3) shear-induced mixing resulting from instability of the NLLJ. A weakly stable residual layer provides the conditions for wave activity during Episode 1. This residual layer is eroded by a developing NLLJ from top down during Episode 2. The sustained increase in winds at hill top levels – attributed to the NLLJ – continue to disrupt the CAP through Episode 3. Although cooling is interrupted, the CAP is never completely eroded during the night. Complete CAP breakup occurs some 3.5 h after local sunrise.

This case study highlights a number of meteorological phenomena that can disrupt CAP evolution even in ideal CAP conditions. These processes are unlikely to be sufficiently represented by current operational weather forecast models and can be challenging even for high resolution research models.

KEYWORDS

stable boundary layer, complex terrain, cold air pools, gravity waves, Kelvin-Helmholtz instability, nocturnal low-level jet, COLPEX

1 | INTRODUCTION

Cold air pools (CAPs) are typically characterised by very strong near surface temperature inversions which start to form around sunset within convex terrain such as hollows, valleys or basins. As the CAP grows it spreads out laterally up the slopes with isentropes initially parallel to the valley floor. Without interruption by increasing wind speed, incoming cloud or fog, the CAP can be maintained through the night and temperature differences across the valley or basin depth will continue to grow until sunrise (Gustavsson *et al.*, 1998). Except for the most extreme cases, where CAPs persist for multiple days (Whiteman *et al.*, 2001; Lareau *et al.*, 2013), the CAP will weaken and/or break up during the morning transition as the convective boundary layer is established.

The motivations for studying CAPs are numerous. The formation of CAPs can lead to the heightened risk of prolonged low temperatures, persistence of lying snow, frost, fog and/or pollution episodes (Lareau *et al.*, 2013). Their occurrence can have impacts on the environment, health, road safety (Bogren *et al.*, 2000) and agriculture (Lindkvist *et al.*, 2000; Madelin *et al.*, 2005), with subsequent impacts on the economy; mainly through disruption of transport networks and by damage to crops. The issuing of hazard warnings (such as black ice, extreme cold weather, pollution episodes) and taking action to mitigate these hazards (i.e., gritting roads, activating extreme cold weather and/or air quality action plans), depends on the ability of weather forecast models to accurately predict CAPs. The improved representation of CAPs in weather models is likely to be achieved through either; (1) the continued development of downscaling techniques (Pozdnoukhov *et al.*, 2009; Sheridan *et al.*, 2014, 2018), (2) the development of parameterisations, (3) through increased resolution (Vosper *et al.*, 2013; Hughes *et al.*, 2015). In the short term options (1) and (2) are more practical given that current operational weather forecast models have horizontal resolutions > 1 km. Such models will not resolve CAPs over smaller scales (Vosper *et al.*, 2013), which are typical across the UK. In addition, a well developed CAP parameterisation or downscaling technique applied to regional and global climate models, can subsequently improve the representation of minimum and maximum temperature, which are proxies for the impact of climate change (Daly *et al.*, 2010).

Depending on time, location and atmospheric stability, CAP formation tends to be associated with two regimes; (1) the down-slope drainage of cool air into the valley or basin, referred to as katabatic winds (Heywood, 1933; Manins and Sawford, 1979) or drainage flows (Gudiksen *et al.*, 1992); (2) a sheltered decoupled layer in the lowest part of the valley or basin, where cooling occurs in-situ through a divergence in the sensible heat flux with little or no horizontal advection of cold air (Vosper and Brown, 2008). Both downslope drainage flows and sheltered cooling regimes can occur independently or simultaneously. In the latter instance the colder decoupled layer may be topped by a thermally driven downslope drainage flow layer (Clements *et al.*, 2003; Vosper *et al.*, 2014). There may also be flow within the

cold decoupled layer due to along-valley horizontal temperature gradients giving rise to a pressure gradient driving down-valley flow (Vosper *et al.*, 2014). For complex terrains where valleys meander and join other tributary valleys, down-valley flows are likely to be important in terms of the redistribution of cold air across the valley system (Vosper and Brown, 2008).

The modelling study of Vosper and Brown (2008) and observational analysis by Sheridan *et al.* (2014) and Jemmett-Smith *et al.* (2018) have shown that the variability in ambient wind speed and the radiative conditions mostly determine CAP strength for a given night. Others have also shown that changes in ambient wind speed (Orgill *et al.*, 1992) and direction (Coulter *et al.*, 1989) affect the structure of the flow in valleys, which will subsequently affect the dynamics of the CAP as a whole. Downslope drainage along the upper slopes of a valley are greatly influenced by the large-scale ambient wind and are susceptible to breakdown through turbulent mixing from above, due to their proximity to the free atmosphere, lack of terrain sheltering and generally weaker density gradients than within the valley (Barr *et al.*, 1989; Gudiksen *et al.*, 1992). Orgill *et al.* (1992) found that drainage flows are especially susceptible to erosion by turbulent mixing when above-valley winds exceed 5 m s^{-1} and accelerations exceed $4 \times 10^{-4} \text{ m s}^{-2}$. Similarly, Heywood (1933); Barr *et al.* (1989); Gudiksen *et al.* (1992); Iijima *et al.* (2000); Bogren *et al.* (2000); Whiteman *et al.* (2001); Vosper and Brown (2008) found threshold ambient wind speeds for the existence of CAPs and downvalley flows between 5 and 8 m s^{-1} . Without changes in the radiative conditions these studies suggest that both CAPs and down valley drainage flows are greatly influenced when ambient winds exceed a critical value so that reduced stability allows top down erosion by shear-driven turbulence.

Zängl (2008) suggested that CAP erosion by turbulent mixing from above plays a comparatively minor role in deep valley systems, which often have complex wind regimes and where CAPs can persist for multiple days (Whiteman *et al.*, 2001). Therefore it seems entirely plausible that turbulent mixing from above – potentially caused by a number of stable boundary layer (SBL) phenomena – will play a comparatively larger role in valleys with shallower depths compared to large deep mountainous valleys or basins. Mahrt and Heald (2015) showed the intermittent destruction of shallow valley CAPs (or “marginal cold pools”) as a result of relatively small increases in wind speed of a few metres per second.

This paper presents a case study of CAP evolution using an unusually extensive set of field measurements collected as part of the COLd-air Pooling EXperiment (COLPEX) (Price *et al.*, 2011). The experiment took place from July 2009 to April 2010 around the Clun Valley in Shropshire, UK. This is a region of hilly terrain with multiple valleys typically of depth 200 m or less. The valleys in the study area are deeper than in the study by Mahrt and Heald (2015), yet much shallower than many other CAP studies in mountainous regions (e.g. Whiteman *et al.*, 2001; Zängl, 2008; Lareau *et al.*, 2013). Jemmett-Smith *et al.* (2018) undertook a short climatological study of CAPs and drainage flows during COLPEX. This was an unusually cold winter with record low NAO index, however the study highlighted how common these events are in this region, and also the conditions conducive to CAP formation. The synoptic conditions during the case study investigated here were ideal for CAPs to form; high pressure, clear skies and light ambient winds. Despite this the CAP that formed was disturbed on several occasions during the night. The objective of this paper is to (i) give an overview of the CAP using measurements of near-surface wind and temperature and (ii) understand the reasons for CAP disruption during three notable episodes, during otherwise ideal conditions using observations from radiosondes and Doppler lidar. A description of data and methods are given in section 2. Section 3 presents results and discussion of each episode in turn. A summary and conclusions are given in section 4.

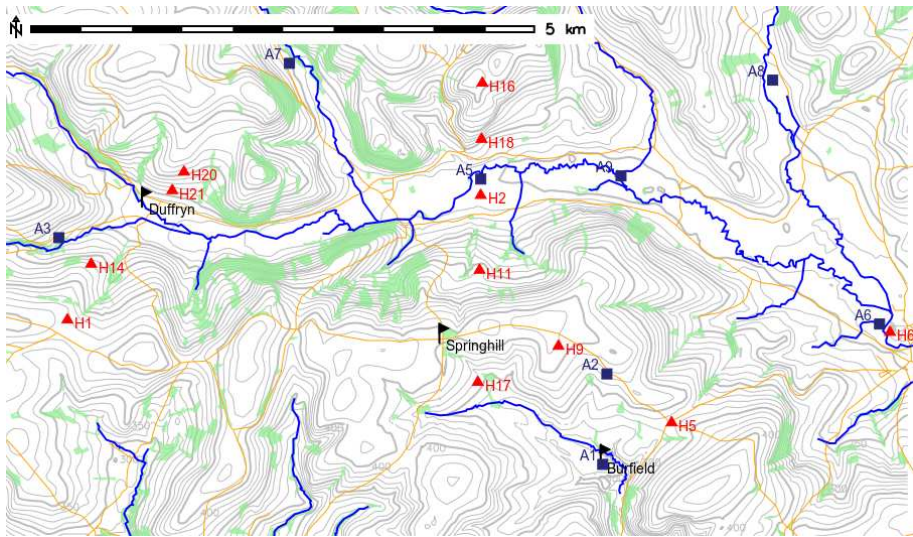


FIGURE 1 Map showing instrumentation deployed during COLPEX. Red triangles mark HOBO temperature / humidity loggers, dark blue squares are automatic weather stations (AWS) and the main mast sites (Burfield, Duffryn and Springhill) are highlighted by black flags. The HOBO loggers and AWS are labelled H and A, respectively. Height contours are plotted every 10 m, with thicker labelled contours every 50 m. Rivers are shown with blue lines, roads with yellow lines and woodland with light green shading. Map data is ©Crown copyright and Database Right 2018. Ordnance Survey (Digimap License).

2 | DATA AND METHODS

A key part of the COLPEX experiment was to improve our understanding and enable prediction of temperature patterns and local flows in complex terrain, caused by the formation of cold-air pools in valleys during stable night-time conditions, given accurate knowledge of the large scale meteorological conditions (Price *et al.*, 2011). The COLPEX project involved an extensive field experiment conducted in the Clun Valley (52.43°N, 3.14°W), which is located within the county of Shropshire, on the border between England and Wales. A map showing the terrain and instrument locations is given in Figure 1. The rolling hills and network of valleys that make up the Clun Valley typify many regions across the UK and elsewhere in the world. The terrain is modest with valley depths rarely exceeding 250 m. The main axis of the Clun Valley is roughly orientated west-east and is ~25 km in length. At the centre of the Clun Valley, north of Springhill (Figure 1), the floor width is approximately 0.5 km and the peak to peak width approximately 1.5 km. The neighbouring Burfield Valley, located just south of the Clun Valley, is approximately 15 km in length and is mostly orientated north-west to south-east. The ground cover in these valleys is largely green pastures lined with hedgerows and less than 10% woodland.

A detailed description of the instruments deployed is given in Price *et al.* (2011). Here just the relevant key features are summarised. Most instruments were deployed from at least September 2009 to April 2010. Three main sites, which include instrumented masts taking measurements of mean flow and turbulent fluxes up to 30 or 50 m, were located in the Burfield valley (~316 m ASL), Upper Duffryn in the Clun valley (~246 m ASL) and Springhill Farm (~402 m ASL); in future these mast sites are simply referred to as Burfield, Duffryn and Springhill. Duffryn is located on the floor of the main Clun Valley roughly 5.5 km SE from the valley head. Burfield is located within a bowl shaped area in the northern

TABLE 1 Location and altitude above sea level of the main sites and the HOBO loggers and AWS used in the analysis.

Site	Type	Description	Altitude (m)
Duffryn	Main site	Floor of Clun valley	246
Springhill	Main site	Hilltop (south of Clun valley)	402
Burfield	Main site	Floor of Burfield Valley	316
A2	AWS	Hill top (south of Clun valley)	376
A5	AWS	Floor of Clun valley	204
A7	AWS	Floor of side valley	253
H6	HOBO	Floor of Clun valley (down valley)	186
H2	HOBO	Floor of Clun valley, next to A5	202
H16	HOBO	Hill top (north of Clun valley)	362

part of the Burfield Valley. The Burfield site is located higher than much of the Clun Valley floor, including Duffryn. Springhill is sited on a hill top between Burfield and Duffryn. During intensive observation periods (IOPs), radiosonde measurements were launched from Duffryn. At Duffryn a Halo Photonics 1.5 micron pulsed doppler lidar operated by the National Centre for Atmospheric Science (NCAS) gave vertical profiles of backscatter and vertical velocity every minute, with hourly scans to give vertical profiles of horizontal wind. Also deployed throughout the region were 31 satellite weather stations, made up of 21 HOBO data loggers (Onset Computer, inc.) measuring temperature and humidity, and 10 automatic weather stations (AWS; developed and maintained by NCAS and the University of Leeds). In addition to temperature and humidity, the AWS measured horizontal winds (using a 2-D Gill windsonic) and pressure, allowing for a more detailed study of the flow dynamics in the Clun valley. Table 1 lists the sites used in the analysis below, along with a brief description of their location and altitude above sea level. AWS A5 and HOBO H2 and H16 form a transect across the Clun valley, just downstream of Duffryn. AWS A7 is on the floor of a side valley close to A5. HOBO H6 is the site furthest down the Clun valley and lowest in altitude.

This study is focused on measurements obtained during IOP 16 from 4–5 March 2010. The same IOP was used by Vosper *et al.* (2014) in their modelling study. Vosper *et al.* (2014) compared the model with observations and showed that while the model captured the broad development of the cold pool, the observations showed much more variability in cold pool strength during the night (see in particular their figure 2). In addition, the cold pool remained strong until dawn in the observations, while the model had a decreasing temperature difference between Duffryn and Springhill in the later part of the night. Using the COLPEX field measurements this case study aims to gain insight into CAP evolution under “ideal” CAP conditions; light winds, high pressure and little or no cloud cover. In particular, it aims to understand the factors which can disrupt “ideal” CAP development, which are not being captured even in high resolution numerical simulations.

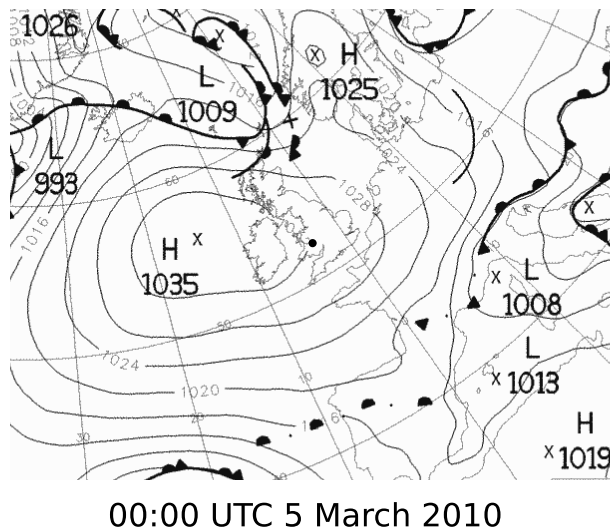


FIGURE 2 Met Office surface analysis chart for 00:00 UTC on 5 March 2010. The Clun Valley region is highlighted by the filled circle.

3 | RESULTS

3.1 | Overview of IOP 16; 4–5 March 2010

IOP 16 took place between 12:00 UTC 4 March and 12:00 UTC 5 March 2010. The weather over the UK was dominated by an anticyclone located off the west coast of Ireland (central pressure 1035 hPa, Figure 2), which led to light winds and clear skies throughout the night. The anticyclone centre moved slowly eastward towards Ireland throughout the IOP and the low pressure to the north of Scotland moved slowly southwards off the east coast of the UK. This led to an increase in pressure of ~ 5 hPa at the hill top site AWS 2 (Table 1; Figure 1) over the 24 h period. There was also a slight increase in the geostrophic wind through the night and a shift towards a slightly more northerly wind direction (from the Met Office operational 4km UK model, but a similar trend is seen from in-situ tower and lidar measurements shown below). Sunset on 4 March was at 17:57 UTC and sunrise on 5 March at 06:50 UTC.

IOP 16 proved to be one of the strongest CAPs observed during COLPEX (in terms of the observed maximum difference between hilltop temperature and valley bottom temperature recorded during the night-time) and the strongest seen in March. The largest diurnal range in potential temperature (θ) measured by the AWS was ~ 14 K at the Clun Valley floor site AWS 5 (Table 1; Figure 1). The smallest diurnal range in θ was 7.7 K at the hill top site AWS 2. The minimum θ value of 265.2 K at AWS 5 occurred soon after local sunrise (06:50 UTC). Note HOBOS do not take measurements of pressure, which is needed for in-situ calculations of θ , and so where θ is required at the HOBOS the pressure was calculated using the hydrostatic equation, the pressure at the nearest AWS and the height difference between HOBOS and AWS. To apply the hydrostatic equation the scale height was calculated using the temperature at the HOBOS and a representative molecular mass for air. Differences due to water vapour were neglected as they are not significant for the small height corrections involved. In-field observations taken at Duffryn reported clear skies, bright stars and small amounts of cirrus seen on occasions up until 00:31 UTC. At 05:35 UTC the ground was frozen hard with a medium deposition of frost on the grass and clear skies with small amounts of cirrus on the horizon.

Temperatures below 0°C were measured by all AWS during the night; therefore, ground frost seems likely across the entire Clun Valley region, with increasing likelihood as the night progressed. By 09:00 UTC it was sunny and clear, with some frost remaining in the shadows. At 11:00 UTC the conditions remained sunny and clear, with no frost present. Minimum visibility measurements at Duffryn and Springhill during IOP16 were 10.9 km and 3.7 km respectively (from Biral HSSVPF-730 present weather sensors at each site), suggesting no fog or mist formed. Infrared satellite images showed no evidence of high cloud in the region throughout IOP 16 (not shown).

The spatial evolution of the CAP is illustrated by Figure 3, which includes 10-minute mean measurements of 2 m potential temperature, 2 m winds (black arrows), 50 m winds at Duffryn (T1), and 30 m winds at both Springhill (T2) and Burfield (T3) (grey arrows). The evolution of the CAP temperature structure through the diurnal cycle is representative of that observed on other CAP nights. During the afternoon (Figure 3(a)) temperatures are similar across the entire region and valley winds are either up-valley or mirror the ambient wind. During the first stages of CAP formation cold air collects in the bottom of the valleys first. At a similar time the valley winds become decoupled from the ambient wind aloft and turn to down-valley flow (Figure 3(b-c)), which reflects thermally-driven valley flows. The lowest regions remain cooler than locations above, forming a temperature inversion (Figure 3(b-c)), which is sustained until CAP breakup occurs some time after sunrise (Figure 3(d)). The down-valley flows observed throughout the night cease to exist following CAP breakup (Figure 3(d)).

A more detailed view of the temporal evolution of the cold pools at several sites during IOP 16 is shown in Figure 4. At all locations cooling starts ~2 h prior to local sunset (Figure 4(a)). By ~19:00 UTC (~1 h after local sunset) the valley sites are all clearly colder than Springhill indicating a temperature inversion, with the lowest temperatures at HOBO 6, which is the furthest down the Clun Valley and has the lowest altitude. Temperatures in the shallower Burfield valley and in a tributary of the Clun Valley (AWS 7) are slightly higher than in the main Clun Valley. The inversion persists until ~09:00 UTC the following morning (local sunrise 06:50 UTC) when temperatures across all sites become similar. A weak CAP remains in some of the lowest regions at 10:00UTC, ~3 h after local sunrise, (Figure 4(a)), with the lowest sites (HOBO 6, AWS 5) remaining slightly cooler than those above.

The valley environmental lapse rate (ELR), defined as the temperature gradient, dT/dz , over the valley depth, provides a quantitative measure of the strength and development of the CAP. Two ELRs are shown in figure 4(b); the first is a near-surface temperature lapse-rate calculated using linear regression of all 10-minute averaged 2 m HOBO and AWS temperature data, the second is a boundary-layer ELR calculated by linear regression of the Duffryn radiosonde temperature data between 0 and 200 m AGL. Consistent with Figure 4(a), the ELR shows the evening transition from a well-mixed convective boundary-layer (negative ELR) to a stable nocturnal boundary layer (positive ELR) around sunset. From sunset until ~22:00 UTC the ELR increases uninterrupted, reflecting undisturbed growth of the CAP. However, during the periods 22:00-23:30 and 02:30-03:30 the ELR decreases with a recovery in between. From ~04:00 UTC there is a rapid strengthening of the CAP, with an overnight maximum around sunrise at ~06:50 UTC. After sunrise the ELR rapidly decreases, becoming negative ~2.5 h after sunrise. Overnight the ELR from the radiosonde measurements is typically (but not always) higher than the ELR from the 2 m temperatures, reflecting the fact that the air at hill top sites is cooler than the air above Duffryn at a similar altitude due to a local stable boundary layer at the hill surface (Sheridan *et al.*, 2014).

Relative humidity (RH; Figure 4(c)) and water vapour mixing ratio (M_r ; Figure 4(d)) measurements from a valley floor site HOBO 2 (202 m ASL, co-located with AWS 5) and a hill top site HOBO 16 (362 m ASL) also change during the IOP. These sites are chosen because; (1) they form part of the same transect of measurements, (2) they represent locations at different altitudes, (3) both have reliable and continuous measurements throughout IOP 16. Unfortunately humidity data from AWS 5 and AWS 7 were not available on this night due to problems with the sensors. Before sunset, RH and M_r are similar at both locations. From 16:00 UTC until sunset (~18:00 UTC) RH increases, while M_r remains

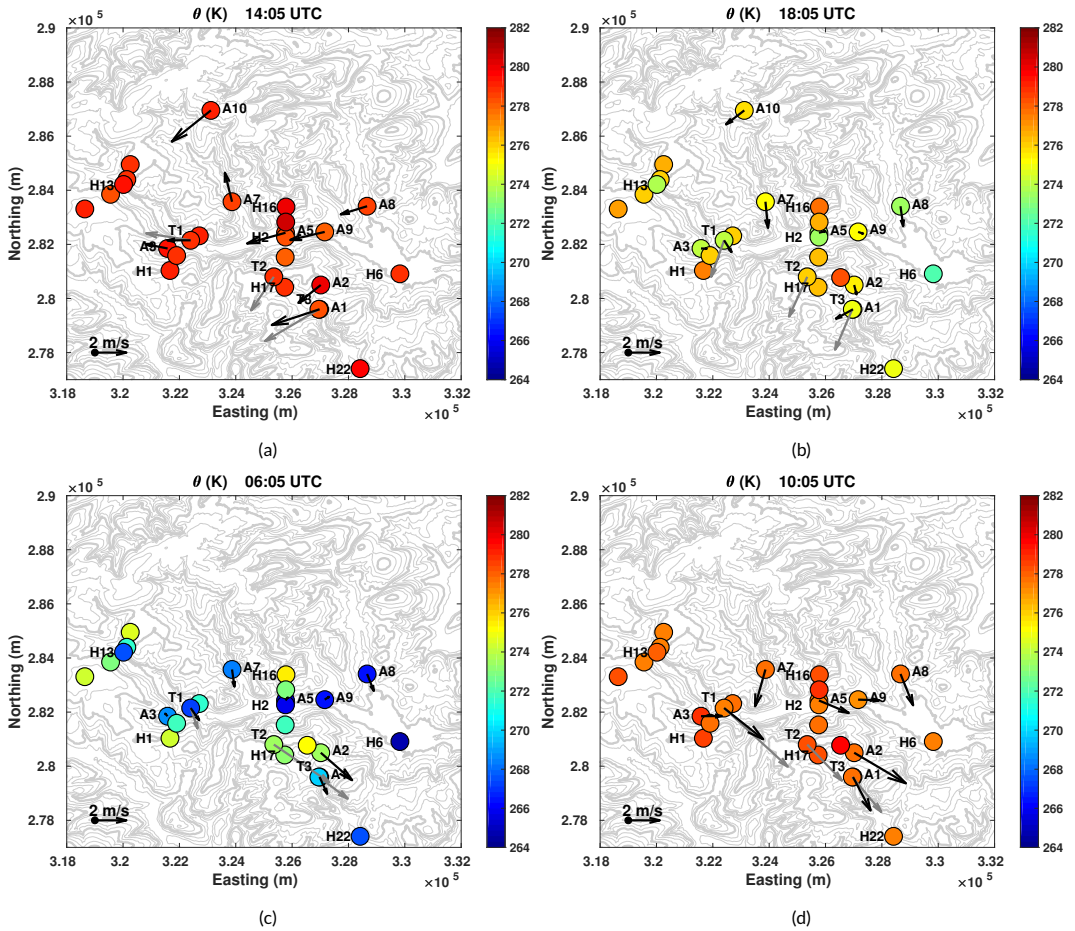


FIGURE 3 2 m potential temperature, 2 m winds (dark arrows), 50 m winds at Duffryn (T1), 30 m winds at both Springhill (T2) and Burfield (T3) (grey arrows). Data are 10 min mean periods centred at: 14:05 UTC, 18:05 UTC, 06:05 UTC and 10:05 UTC. Wind direction is vector averaged and the magnitude is the mean wind speed (scalar). Height contours are plotted every 25m, with a thicker contour every 100m. Map data is ©Crown copyright and Database Right 2018. Ordnance Survey (Digimap License).

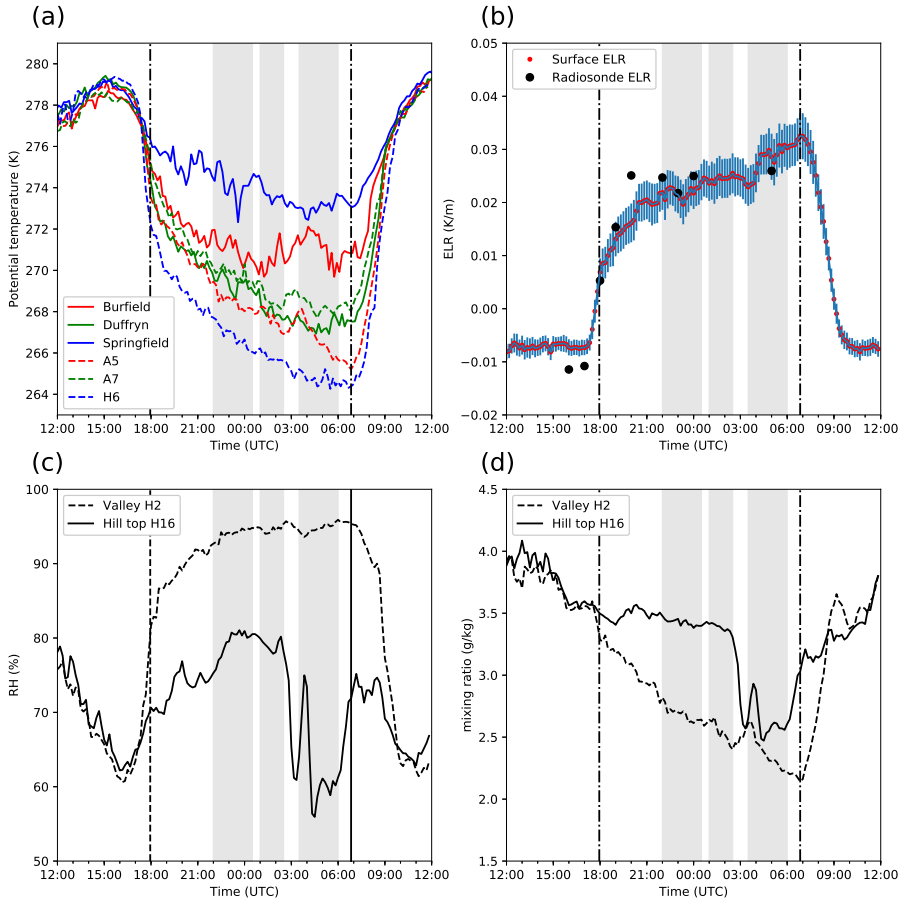


FIGURE 4 24 h time-series of (a) 2 m potential temperature, (b) environmental lapse rate (ELR), (c) relative humidity (RH), (d) water vapour mixing ratio (M_r) at various sites. In (b) the red points are the near-surface ELR calculated using all AWS and HOBO 2 m temperature measurements and the black circles show the ELR obtained using radiosonde measurements from Duffryn (0–200 m AGL, above ground level). The error bars on the ELR show one standard deviation of the uncertainty in the estimate of the near-surface ELR based on the linear regression. Vertical dashed lines indicate the time of local sunset and sunrise. The grey shading denotes the three episodes discussed. The location and altitude of the AWS, HOBO and tower sites are given in Figure 1 and Table 1.

relatively constant. This increase in RH is primarily caused by falling temperatures (Figure 4(a)). After sunset M_r at the hill top site remains relatively constant until ~03:00 UTC, and RH increases as the air cools. In contrast, M_r at the valley floor site decreases steadily through the night. Despite this, the stronger cooling at the valley floor site leads to a much more rapid increase in RH. A notable peak in RH occurs around 02:30 UTC, reaching ~95% at the valley floor and ~80% at the hill top, this coincides with the peak in ELR. Over the following hour (02:30 to 03:30 UTC) a dramatic drop in M_r occurs at the hill top (HOBO 16) and values briefly match those seen at the valley floor (HOBO 2). This coincides with a decrease in ELR; further discussion of this period will follow. From 04:00 to 07:00 UTC, RH changes little at the valley floor (HOBO 2) remaining around 95% and M_r continues to fall reaching a minimum around sunrise (~06:50 UTC). After sunrise values of RH and M_r at the hill top and valley floor site begin to converge. Around 10:30 UTC RH and M_r return to values seen before sunset the previous evening. Other comparable sites show a similar pattern of RH and M_r changes. The fact that M_r drops continuously in the valley but remains relatively unchanged until 02:30 UTC at the hill top suggests that the moisture at the valley bottom site is being continuously removed through much of the night by either frost or dew deposition as the air pools along the valley floor. Frost deposition seems more likely given that air temperatures at the lowest sites reach freezing around sunset and continue to cool thereafter. Ground temperatures are expected to be colder still (see Vosper *et al.*, 2014). As noted in section 3.1, frost deposition was observed at Duffryn later in the night. Frost deposition would also explain why the RH values (with respect to water) level out at a constant value slightly less than 100% as the saturation vapour pressure with respect to ice is slightly lower than the saturation vapour pressure with respect to liquid water. The difference is however close to the accuracy of the sensors (error up to 4.5% in RH at 100% RH, typically < 3.5% from 10–90% RH). In contrast, except for a brief fall to ~0°C at ~04:00 UTC, temperatures at the hill top site HOBO 16 remain around 1°C for much of the period between 00:00 and 07:00 UTC, an indication that ground frost was likely, but not necessarily prevalent there in the early hours.

One notable feature of Figure 4(a) is the numerous intermittent warming (or mixing) events that occur amid an overall cooling trend. The smaller intermittent events are similar in scale to the averaging period (10 minutes). These are likely to be caused locally by one or more of the mechanisms outlined by Banta *et al.* (2004): (a) local shear, (b) local flow pulsations, (c) local obstacle effects, (d) the convergence or divergence of local drainage flows, (e) gravity waves. An example of a larger warming (or mixing) event occurs at Burfield between 03:00 and 04:00 UTC. At times these warming events are seen across several sites, possibly with some time lag, suggesting events propagating across the region. These warming events may also be accompanied by drying of the air, such as the decrease in M_r at HOBO 16 (Figure 4(c-d)); although valley floor locations such as HOBO 2 (co-located with AWS 5) are generally unaffected by these changes. These warming events also lead to changes in the ELR (Figure 4(b)). Lidar measurements taken at Duffryn (Figure 5) show a number of anomalies occurring at and above hill top height that occur at a similar time to these thermodynamic changes. Three episodes of disruption (Episodes 1, 2 and 3) are identified based on changing characteristics of the lidar measurements (Figure 5) and ELR (Figure 4(b)). These three episodes comprise the focus of the following sections, with the aim of understanding what caused the anomalies and how they relate to the disruption of the CAP evolution. The changes in lidar and ELR characteristics are often gradual and so there is some subjectivity in precisely where the episodes start and end. The episodes serve primarily to highlight different types of behaviour which occur during the night.

3.2 | Episode 1; wave activity

Episode 1 occurred between 22:00 and 00:30 UTC (Figure 5) and is characterised by a number of increases and decreases in the lidar vertical velocities that occur in the region at and above the hill tops near Duffryn (200 to 400 m AGL). The periodic behaviour in the lidar vertical velocities is unlike anything seen at other times during IOP 16. Concurrent with

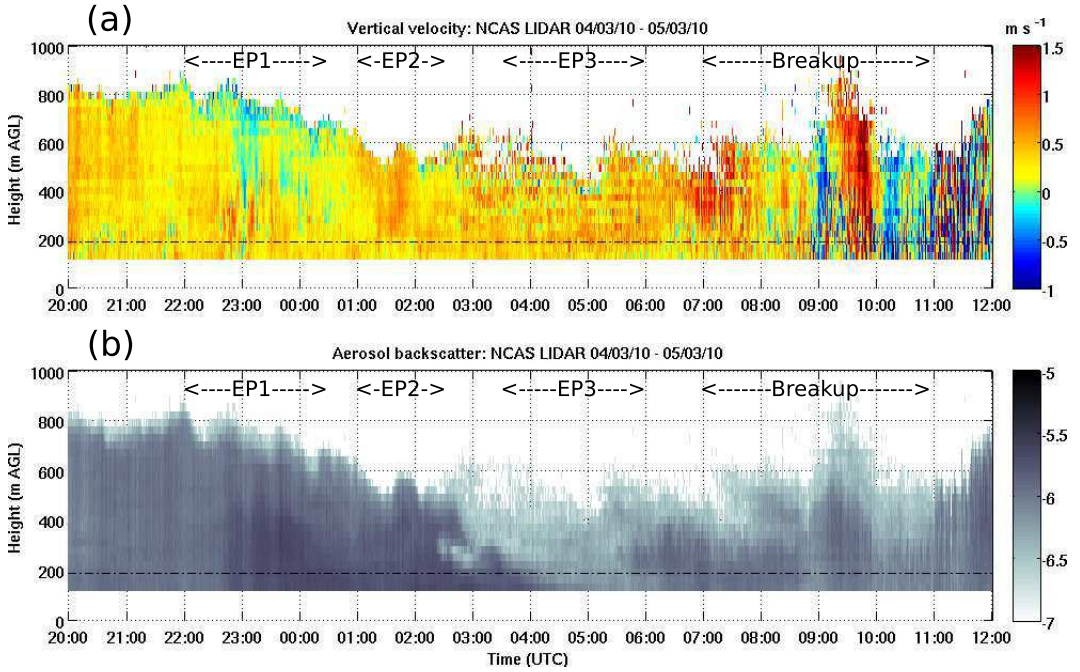


FIGURE 5 Time series of NCAS lidar measurements taken at Duffryn showing vertical profiles of (a) vertical velocity and (b) backscatter. The vertical dashed lines indicate local sunrise. The horizontal dot-dashed line marks the mean hilltop height.

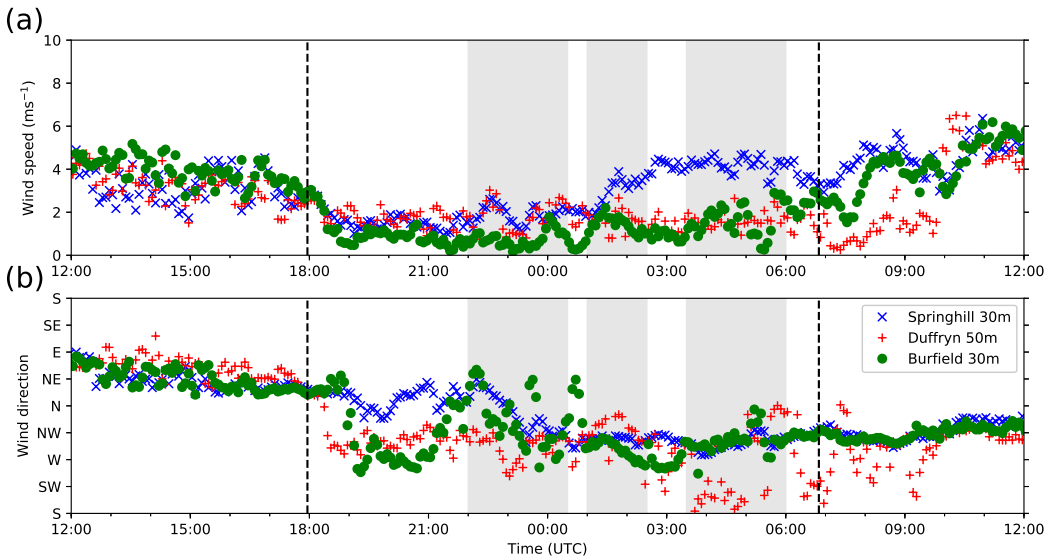


FIGURE 6 Time series of (a) wind speed, and (b) wind direction, measured at the tower sites Burfield 30 m (346 m ASL), Duffryn 50 m (296 m ASL) and Springhill 30 m (432 m ASL). The vertical dashed lines mark sunset and sunrise. The grey shading denotes the three episodes discussed.

these wave-like motions, an interruption in the CAP growth also occurs across the region, highlighted by the decrease in ELR around 22:00 UTC (Figure 4(b)). Towards the end of Episode 1 the ELR starts to increase again, suggesting a return to CAP growth after the disturbance. This increased lapse rate is due to a combination of continued cooling at lower valleys sites, and warming at hill top sites (see e.g. Figure 4(a)). Unlike the preceding and following periods, the radiosonde-derived ELR at 23:01 is very close to the ELR derived from screen temperature observations on the valley sides.

Prior to Episode 1 there are generally down-valley winds at both Duffryn and Burfield (WNW-NNW and W-NW respectively), consistent with a downvalley drainage flow in the cold pool (Figure 6). The down-valley flow at Burfield is disrupted at the start of Episode 1 (~22:00 UTC) with fluctuations to the NW and NE seen (Figure 6(b)), which coincide with the change in ELR (Figure 4(b)). The down-valley flow at Duffryn appears more persistent compared to Burfield, but there is still a slight change in wind direction between ~22:30 and 23:30 UTC, with winds shifting from the NW at 22:30 UTC to the W, then to the WSW by 23:05 UTC (Figure 6(b)); note that a WSW direction is roughly aligned with the axis of the neighbouring tributary valley containing AWS 3 that joins from the SW (see Figure 1), suggesting that this is the result of a tributary flow encroaching into the main valley. The down-valley flow at Duffryn is re-established by 23:35 UTC and remains for the duration of Episode 1. The lower wind speeds at Burfield compared to Duffryn may partly explain the earlier and larger disruptions to the wind direction.

Radiosonde profiles from Duffryn show changes in the vertical structure of the atmosphere during IOP 16 (Figure 7). The profiles identify a number of different layers: the cold pool, a stable layer above the cold pool around hill top height, a residual layer remaining from the previous day's convective boundary layer and topped with a capping inversion, and then the free troposphere above. Three of the profiles occur during Episode 1. The 22:02 UTC radiosonde profile at the start of Episode 1 shows the existence of a residual layer extending from the hill tops at ~200 m to around 700 m AGL. This residual layer has a relatively constant potential temperature and is capped by a temperature inversion and

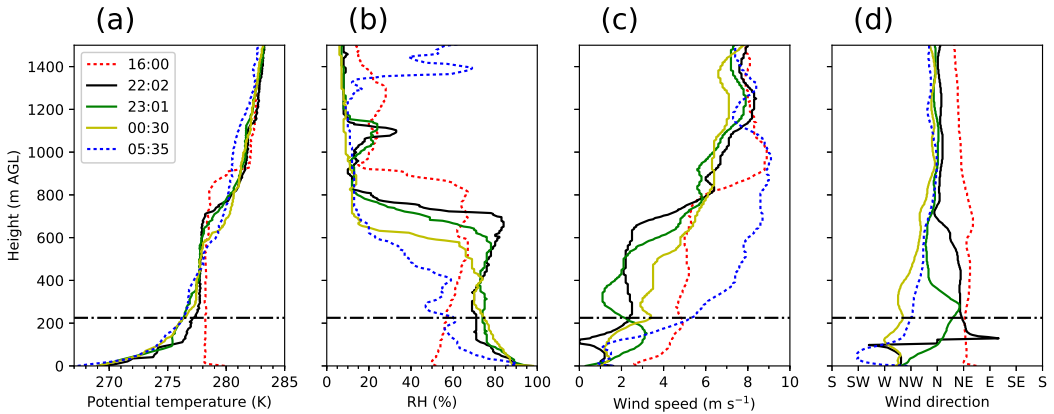


FIGURE 7 Radiosonde profiles launched from Duffryn at 16:00, 22:02, 23:01, 00:30 and 05:35 UTC, showing: (a) potential temperature, (b) RH (%), (c) wind speed (m s^{-1}), (d) wind direction.

a very dry air mass above (RH is typically between 5 and 20% above 800 m). Over episode 1 the top of the residual layer descends, either due to large scale subsidence in the high pressure or due to mixing from above. The fact that the inversion becomes less sharp over time suggests that mixing is at least partly responsible, as subsidence alone would be expected to sharpen the inversion. The layer between 100 m and 400 m AGL cools and becomes more stable during episode 1. This cooling at the hill tops relative to the valley bottom is consistent with the decrease in ELR seen in Figure 4(b). In all profiles the wind direction in the lowest 50 m AGL is predominantly down-valley (NW), agreeing well with measurements made at Duffryn (Figure 6) and winds above 800 m AGL are northerly. In between however there are significant differences in wind direction between soundings and this is an important aspect of episode 1. The 22:02 sounding shows WNW / W winds in the lowest 100 m within the cold pool, rapidly changing to ESE then NE above the cold pool, before backing slowly to N around 700 m. In contrast at 23:01 the winds steadily veer with height to NE at around 250 m, before backing to NNW around 400 m. By 00:30 the wind direction becomes less variable with W winds around 50 m AGL slowly veering to N around 800 m AGL. The changes in wind direction at hill top height are corroborated by measurements at Springhill (Figure 6), which back from NE at 22:35 UTC to N by 23:35 UTC and W at 00:30.

The ascent rates of the radiosondes launched from Duffryn (Figure 8) corroborate the picture of wave activity around 23:00 UTC. The ascent rate at 23:01 UTC (Figure 8(b)) shows short vertical wavelength oscillations in the ascent rate below about 400 m, consistent with the lidar observations. There is also a clear oscillatory structure between about 2 and 5 km. Both of these features are absent in the soundings at 22:02 and 00:30 UTC (Figure 8(a) and (c)). Whether or how these different scale features are linked is unclear. There is little evidence from the soundings of large changes in θ (and hence the buoyancy of the balloon) and so these ascent rate changes are likely due to changes in vertical velocity from gravity waves. Figure 8(e) shows the Scorer parameter, l ($l^2 = N^2/u^2$, ignoring the small curvature term) for each of the 4 soundings. To reduce noise in the profiles, particularly when calculating gradients, the 2 s radiosonde data is sub-sampled to 20 s (roughly 50 m in the vertical). $N^2 = (g/\theta_0)(d\theta/dz)$ and u are calculated locally at each point. The Scorer parameter can be interpreted as the maximum horizontal wavenumber for which internal gravity waves can propagate. The Scorer parameter has a value of around 3 km^{-1} at 800 m (the height of the oscillations in the aerosol layer top in Figure 5(a)), with decreasing values above this. This value for the Scorer parameter corresponds to a wavelength $2\pi/l \approx 2 \text{ km}$, which is less than or comparable with the scale of the local topography with the separation between

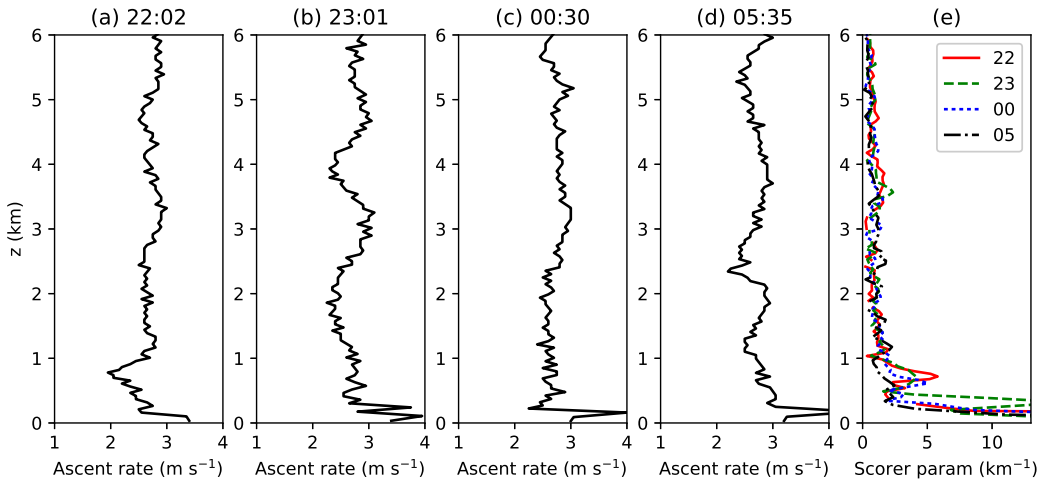


FIGURE 8 Radiosonde rate of ascent for profiles launched from Duffryn at (a) 22:02, (b) 23:01, (c) 00:30 UTC and (d) 05:35 UTC and (e) Scorer parameter at each time.

adjacent valleys or hilltops being of the order of 5 – 10 km. Thus the terrain scale favours the generation of waves which are trapped in the layer beneath this, decaying with altitude above it. From the dispersion equation $m^2 = l^2 - k^2$ for a constant stratification, where k and m are the horizontal and vertical wavenumbers respectively and so m must also be less than the Scorer parameter l . Although there is evidence of a vertical wave-like structure in the 23:01 radiosonde, with a vertical wavelength of approximately 2 km, the associated vertical wavenumber of approx 3 km^{-1} is too large to allow wave propagation based on the Scorer parameter values above 1 km AGL, assuming simple linear hydrostatic wave theory. The wave would be supported at low levels (below 1 km), and so the observations are consistent with the generation of gravity waves by the topography which are then trapped or attenuated above about 1 km in altitude due to the decrease in Scorer parameter.

Other than a secondary maximum in the Scorer parameter around 400 m due to the wind speed minimum at this level, the Scorer parameter profiles are quite similar for all the soundings. The Scorer parameter however only gives information on the capacity to support waves, not on the forcing. It also says nothing about wind direction effects on wave propagation. From the wind speed and direction profiles in Figure 7 there do appear to be differences in the low level wind direction at this time as the wind direction in the residual layer (200 - 800 m) changes from N/NE to more NW. Wind blowing across the valley from a different direction will lead to different forcing which may explain the presence of wave activity at this time, but not in the other soundings, and despite the vertical wavenumber of the waves being apparently too large. The fact that the vertical wavelengths observed are too small to be supported by the observed profile of the Scorer parameter may be another reason that the waves are not seen during other periods of the night.

Figure 9 shows the evolution of the stability between the valley floor and hill tops during IOP 16 in terms of the Bulk Richardson number (Ri_B) (Stull, 1988). Ri_B is calculated for a layer between Springhill 30 m AGL and either Burfield 30 m AGL or Duffryn 50 m AGL. Using 10-minute mean data separated into 1 h blocks, Ri_B is calculated here as;

$$Ri_B = \frac{N^2}{(\Delta U / \Delta z)^2} \quad (1)$$

$$N^2 = \frac{g}{\theta} \frac{\Delta\theta}{\Delta z} \quad (2)$$

$$\Delta U = \sqrt{(u_2 - u_1)^2 + (v_2 - v_1)^2} \quad (3)$$

where, N^2 , is the Brunt-Väisälä buoyancy frequency, ΔU , is the magnitude of the velocity difference between the two measurement sites, Δz , is the height difference and $\Delta\theta$, is the difference in potential temperature. As before, Springhill (30 m AGL = 432 m ASL) represents the ambient flow above the valleys. Burfield (30 m AGL = 346 m ASL) and Duffryn (50 m AGL = 296 m ASL) represent flow within the valley interior at their respective sites. Values of $Ri_B > 1$ represent laminar flow (strong stability), for $0.25 < Ri_B < 1$ the layer is in transition between laminar and turbulent flow (near neutral), and when $Ri_B < 0.25$ the flow is unstable and likely to become or remain turbulent. In the early stages of CAP evolution and during Episode 1, the region between the hill top site Springhill and the valley site Duffryn is laminar (Figure 9(b)). The same is not true for Springhill and Burfield. For half of the 1 h period between 22:00 and 23:00 UTC, the region between Springhill and Burfield is in transition between laminar and laminar/turbulent flow. This indicates that the shallower Burfield Valley is more susceptible to turbulent mixing penetrating down into the valley during Episode 1 compared to the period immediately beforehand. The intermittent changes in lidar vertical velocity above hill top height may be an indication of Kelvin-Helmholtz instability generating this mixing. Although the lidar cannot measure within the valley, the Ri_B values suggest that the mixing is not likely to penetrate down into the valley at Duffryn at this time.

To summarise, lidar and radiosonde results show evidence of wave activity at and above the hill top level during Episode 1 (Figures 5 and 8). Associated with this is a marked change in the winds near hill top and through the residual layer (Figure 7). We hypothesise that these changes lead to mixing and a disruption in the cooling rate within the cold pool (Figure 4). For most of Episode 1 the lidar shows relatively shallow vertical motions (only extending a few hundred metres above the valley top at most), suggesting they may originate locally from relatively low levels. There are a number of different processes which may generate these wave-like motions, including:

- Propagating waves on the interface of the cold pool, possibly generated through Kelvin-Helmholtz instability.
- Stationary waves forced by the surrounding topography.
- Downslope flow with a hydraulic jump leading to the forcing of Stationary waves located over the valley (e.g. Renfrew, 2004; LARGERON *et al.*, 2013)

The changes in wind speed and direction over this period would lead to the location and magnitude of any stationary wave changing with time, leading to the variations in vertical velocity seen above the lidar.

3.3 | Episode 2; Acceleration of ambient wind

During Episode 2 (between 01:00 and 02:30 UTC), increases in vertical velocities ($\sim 0.7 \text{ m s}^{-1}$) are seen in the lidar profiles (Figure 5) that descend with time from 600 m AGL at 01:00 UTC, reaching the hill top level by 01:30 UTC before dissipating around 02:00 UTC. As in Episode 1, a wave like structure is seen at the top of the aerosol layer during Episode 2, accompanied in its upward phase by a strengthening updraft above hill top height. On this occasion, however, the intermittent behaviour in the 2m temperatures linked with wave activity in the previous episode is absent. The episode is again characterised by a relatively constant ELR based on screen temperatures on the valley sides. Unfortunately no radiosonde measurements were taken during Episode 2 and so it is impossible to compare the surface ELR to the

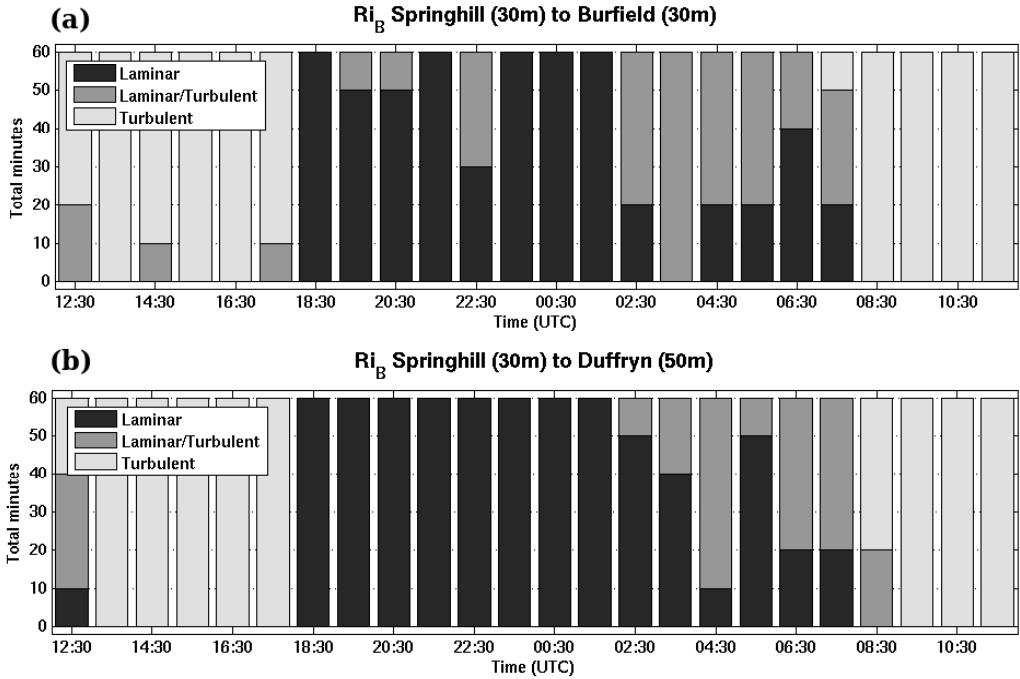


FIGURE 9 Bulk Richardson number (Ri_B) representing the layer between Springhill 30 m AGL and; (a) Burfield 30 m AGL, (b) Duffryn 50 m AGL. The bars show the fraction of the hour in each flow regime: $Ri_B < 0.25$ (turbulent); $0.25 \leq Ri_B < 1$ (laminar / turbulent); $Ri_B \geq 1$ (laminar).

radiosonde ELR, or to look for any evidence of wave activity in the radiosonde ascent rates.

The disturbance in Episode 2 has a relatively small impact on the CAP evolution compared to Episodes 1 and 3. There is some warming in the upper parts of the valleys as seen at Burfield (Figure 4(a)); the small peak in ELR at the end of Episode 2 (02:30 UTC) further supports this (Figure 4(b)). The increase in vertical velocities in Episode 2 coincides with a sudden increase in the wind speed at Springhill from 2 to 4.5 m s⁻¹ between 01:00 and 02:00 UTC (Figure 6). Ambient winds measured at Springhill generally persist below 2 m s⁻¹ from sunset until 01:00 UTC and remain above 3 m s⁻¹ for the remainder of the night after 02:00 UTC. Such changes are likely to affect the stability of the flow around the level of the hill tops.

Figure 9 shows that, for the 3 h period preceding 02:00 UTC the region above Burfield and Duffryn is predominantly laminar; however, for the 1 h period between 02:00 and 03:00 UTC Duffryn becomes partly laminar/turbulent and Burfield predominantly laminar/turbulent. During Episode 2 the upper valley regions appear to be in transition from laminar to laminar/turbulent flow. This occurs at the same time as the increase in vertical velocities is seen descending in the lidar with time (Figure 5) and the rapid increase in ambient winds seen at Springhill (Figure 6). The decrease in stability near the hill top level would be expected to lead to more shear-driven turbulence, mixing warmer air down into the valley interior. Nevertheless ambient winds remain relatively low (less than 5 m s⁻¹) throughout Episode 2 and are lower than the threshold of 5 – 8 m s⁻¹ quoted by other studies as initiating CAP and downvalley drainage flow breakup (Barr *et al.*, 1989; Gudiksen *et al.*, 1992). This suggests that even below such thresholds disturbances may occur which partially disrupt, but do not remove, the cold pool. Such disruption is likely to occur first in the upper parts of the cold pool due to proximity to the free atmosphere and generally weaker density gradients than at the valley bottom. Orgill *et al.* (1992) suggest that ambient wind accelerations exceeding $\sim 4.0 \times 10^4$ m s⁻² can lead to erosion of a downvalley drainage flow. The acceleration of the ambient wind over the 1.5 h period during Episode 2 equates to a mean acceleration of $\sim 4.5 \times 10^4$ m s⁻²; therefore, results here are in-line with findings by Orgill *et al.* (1992).

These thresholds are all empirical and dimensional. A more suitable non-dimensional parameter for the wind speed would be the bulk Richardson number, Ri_B , or the related 'non-dimensional valley depth' used by Vosper and Brown (2008); Sheridan *et al.* (2014). The mechanism by which flow acceleration erodes cold pools was examined in detail using large-eddy numerical simulations by Lareau *et al.* (2015), who found that top-down turbulent erosion led to increased stability at the cold pool top, requiring stronger winds to maintain dynamic instability.

The increase in winds seen at Springhill may reflect the continued trend seen in the radiosonde profiles during Episode 1, where a descent of an inversion associated with a decrease in RH and increase in winds is seen. Although there are no radiosonde launches during Episode 2 to confirm it, it seems likely that the acceleration of the flow is at least in part due to the formation of a nocturnal low level jet (NLLJ) as described by Thorpe and Guymer (1977). The acceleration of the flow in the residual layer is already apparent from the radiosondes in Episode 1. Unfortunately the lidar retrieved wind profiles do not extend high enough to reach the peak of the jet, however they do confirm the increased wind speeds up to a height of at least 400m AGL (Figure 10). In the later 05:35 UTC radiosonde profile there is clear evidence of such a NLLJ, as described below.

3.4 | Episode 3; Nocturnal low-level jet

During Episode 3, from 03:30 to 06:00 UTC, the lidar vertical velocities appear distinctly different to those earlier in the night (Figure 5). The vertical velocities are characteristically more turbulent, with increased values present across the majority of the lidar profile depth (200 to 600 m AGL). The mixing of the residual layer over the night leads to lower aerosol concentrations during Episode 3, and hence a weaker backscatter signal. This may in part explain the more noisy vertical velocity signal, although the data is filtered based on the signal-to-noise ratio, and the increased magnitude of

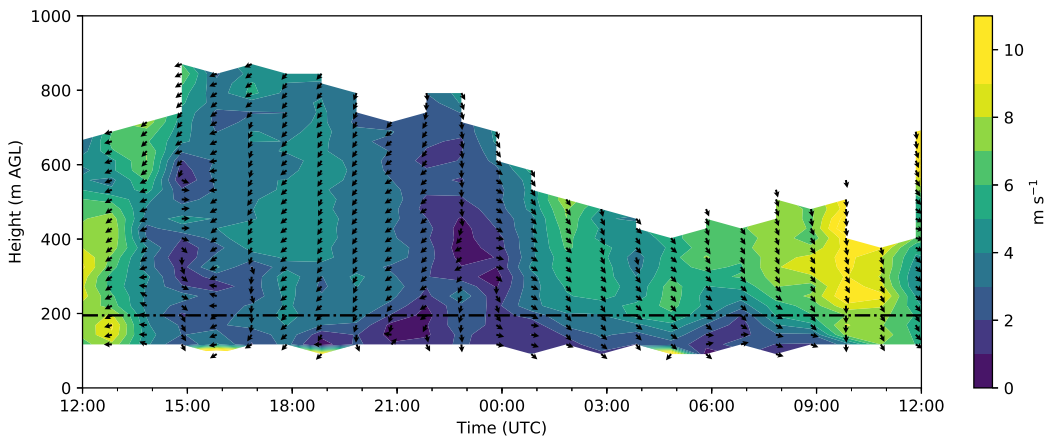


FIGURE 10 Time-height contour plots of horizontal wind speed at Duffryn from the NCAS lidar. The dashed line indicates local hill tops. Arrows indicate wind direction.

the more coherent velocity variations suggests there is also a physical component to this. Episode 3 is also characterised by a steady increase in the surface based ELR throughout the period, unlike both episodes 1 and 2. Only one radiosonde was launched during Episode 3, at 05:35 UTC. This showed a similar ELR to the surfaced based ELR, in contrast to period 1. Following the sudden increase in ambient winds during Episode 2, the winds at Springhill remain between 4 and 5 m s⁻¹ throughout Episode 3 (Figure 6). This is confirmed by the lidar horizontal wind speed profiles in Figure 10, which show the existence of increased wind speeds at heights close to hill top level.

Figure 9 indicates that the flow at both Burfield and Duffryn is more unstable after 02:00 UTC. This reduction in stability is caused by higher winds. It suggests increased vertical mixing, consistent with the larger and more turbulent vertical velocities in the lidar profile time series (Figure 5). Episode 3 is also associated with reduced lidar backscatter (Figure 5), which is indicative of either drier and/or cleaner air being mixed downwards. The RH and M_r time-series in Figure 4(c-d) show an associated reduction in near-surface humidity at Springhill. At the start of Episode 3 there is a noticeable dip in the ELR (~03:30 UTC) and between 04:00 and 06:00 UTC the ELR rapidly increases. This is due to warming of some elevated sites, including Springhill, combined with continued cooling of valley floor locations (see Figure 4(a)). This hill-top level warming and drying is possibly due to warmer, drier air being mixed down from aloft, or due to advection. The profiles in Figure 7 do not show significant low level warming, but they do show significant drying of the profile overnight.

The change in wind speed and direction following Episode 2 and the sustained higher winds during Episode 3 appear to be part of an evolution in the residual layer flow that occurs during the night. The wind speed and direction above about 800 m change little during the night from 22:00 UTC, although the 16:00 UTC sounding suggests that winds were a little more NE the previous day. The lack of significant changes above 800 m indicates the changes in the lower level wind speed are not primarily the result of wider scale synoptic change. The increase in winds and turbulence at lower levels during Episode 2, and continued erosion of the residual layer coincide with a change in behaviour of the Duffryn and Burfield flows, with greater variation in wind speed at both sites, and a greater variability in wind direction at Duffryn compared to the period following sunset (Figure 6). The typical hill top winds during Episode 3 of between 4 and 5 m s⁻¹ are again consistent with previous studies which suggest a threshold between 5 and 8 m s⁻¹ for erosion of a pre-existing CAP. In this case the cold pool was disturbed, but not removed by the increased ambient winds and

cooling of at the valley bottom continued despite the interruption of down valley flow at Duffryn and to a larger extent at Burfield (Figure 6). Mahrt *et al.* (2010) show similar large wind direction shifts in drainage flows on nights when the synoptic flow is more significant (or cooling weaker).

The radiosonde profiles from Duffryn show the development of a jet above the valley during the night (Figure 7). Around hill top (~200 m AGL) the wind speed at 05:35 UTC is $\sim 5.5 \text{ m s}^{-1}$. Above the hill tops there is a strong wind speed gradient with height, reaching a peak of $\sim 9 \text{ m s}^{-1}$ at $\sim 1000 \text{ m AGL}$. This peak of $\sim 9 \text{ m s}^{-1}$ is slightly higher than the geostrophic wind speed estimated from the surface analysis chart in Figure 2. The 05:35 UTC wind profile is characteristic of a jet, with a distinct supergeostrophic wind maximum around 1000 m. This is well above the nocturnal inversion height, and higher than the NLLJ maximum seen in other studies such as (Thorpe and Guymer, 1977). Some definitions of the NLLJ require a local minimum in wind speed above the maximum however this is not immediately obvious from the available radiosonde profiles in this case. One other notable feature of the jet is that the winds back from NE earlier on in the night to more NW just before dawn, as the wind accelerates. While this might be expected at low levels for a “classical” inertial oscillation NLLJ, one would expect to see winds veering over time higher up in the jet (e.g. Thorpe and Guymer, 1977). This suggests that the NLLJ is not purely driven by an inertial oscillation in this case. The precise cause of the jet in this case remains a topic for further investigation. NLLJs are known to form preferentially inland during the night above near surface inversions, when fine weather conditions prevail and little or no cloud cover is present; conditions synonymous with CAP formation. Radiosonde measurements from other IOPs during COLPEX show similar jet features, suggesting that NLLJs frequently occur on nights with CAPs. We hypothesize that it is the increased low-level wind shear associated with the acceleration of the jet throughout the night that drives the increased turbulence observed in the lidar vertical velocity in Episode 3 (Figure 5).

3.5 | CAP breakup

The coldest temperatures experienced during IOP 16 occurred around sunrise (06:50 UTC), and were at the lowest elevated sites (Figure 3(c) and Figure 4(a)). At the same time a 24 h peak in the ELR occurs (Figure 4(b)), suggesting that temperature differences from the valley floor to the hill tops are the largest observed at any time during IOP 16. Warming is seen across all sites between 07:35 and 08:35 UTC, but the rate of warming is higher at valley floor locations (such as AWS 6 and AWS 5). By 08:35 UTC (~1.5 h after sunrise) a CAP still persists at these lower locations (Figure 4), with potential temperature differences on the order of $\sim 6 \text{ K}$ observed between the lowest site HOB0 6 (Clun) and hill top sites such as Springhill. At $\sim 10:00 \text{ UTC}$ values of θ , RH, M_r (Figure 4) and wind speed and direction (Figure 6) all converge, with measurements at the valley bottom matching those at hill top locations. This suggests that the winds in the valley are coupled with the ambient winds above, i.e. the winds in the valley are driven by downward momentum transport of the ambient wind rather than by cold air drainage, consistent with a daytime convective boundary layer (Whiteman and Doran, 1993; Jemmett-Smith *et al.*, 2018).

During the final break up phase of the CAP between 09:00 and 10:00 UTC, increased vertical velocities are seen in the lidar profile above the valley (Figure 5). This includes an initial downdraft followed by a relatively coherent updraft. The lower edge of this updraft observed above the lidar appears to descend with time. This might be the upward part of an eddy in a shear generated mixing layer which is growing with time, or it could be due to advection of a tilted updraft over the lidar site. The former would be consistent with the LLJ (low level jet) shear leading to mixing, while the latter could also be an updraft originating from the surface. (Note: after sunrise we refer to the jet as a LLJ rather than a NLLJ as it is no longer night, and the jet will begin to recouple with the surface as daytime convective boundary layer develops). With a single vertically orientated lidar it is hard to differentiate these two hypotheses. Meanwhile between 150 and 400 m AGL more intermittent turbulence is detected. This signature has some qualitative similarities

to Episode 1. It may reflect vertical motion associated with re-coupling of the valley atmosphere with the air aloft as the stability previously inhibiting vertical motion is removed.

Lidar horizontal wind speed profiles in Figure 10 show a zone of higher winds roughly accompanying the coherent updraft, descending with time between 09:00 and 10:00 UTC. The updraft may be due to a topographically fixed local circulation, or perhaps due to a trapped wave field associated with the increased wind speed (Adler and Kalthoff, 2016, show a recent example of this). This is consistent with the development, and potential mixing down of the LLJ, though no radiosonde profiles were launched after 05:35 UTC to confirm the jet structure aloft. Regardless, it seems clear that the LLJ significantly influences the conditions leading up to, and possibly during, break up of the CAP, with the potential to influence the timing of the latter. The frequent coexistence of LLJs and cold air pools, due to both being favoured by the same meteorological conditions, suggests that the influence of LLJs might be considered a generic part of CAP evolution, at least in settings similar to the Clun valley.

4 | SUMMARY AND CONCLUSIONS

Accurately predicting minimum temperatures associated with the formation, evolution and breakup of CAPs, remains a challenge for weather forecast models. This paper presents a detailed case study of a CAP in small-scale hilly terrain using an unusually detailed set of field observations from the COLPEX field experiment (Price *et al.*, 2011). The synoptic conditions during IOP 16 are highly conducive to stable boundary layer formation (settled high pressure situation, light winds and clear skies throughout the night) and intensive hill / valley temperature contrasts occur overnight creating the impression of an “ideal” CAP case. Close examination of the data, however, shows that the evolution of the CAP is disturbed by several different small-scale or mesoscale processes during the night. In this instance synoptic changes in the winds alone do not appear to be the direct cause of CAP disturbance and no fog or cloud formations were observed throughout the night. The disturbances were not sufficient to cause complete CAP breakup, unlike the marginal CAPs discussed by Mahrt and Heald (2015). Here the CAP growth is arrested and drainage flows intermittently disturbed. These disruptions are particularly visible in the valley ELR and lidar measurements of vertical velocity. Three episodes are highlighted and CAP disturbance attributed to: (1) wave activity (gravity and/or K-H waves), (2) an acceleration of the ambient wind near hill top level and in the residual layer over a period of 1 h associated with the acceleration of a NLLJ and (3) the further development of the NLLJ leading to shear generated turbulence.

The schematic in Figure 11 summarises the sequence of events that occur during CAP evolution throughout IOP 16. Up to Episode 1 the expected sequence of CAP and drainage flow evolution occurs; there is undisturbed growth of the CAP and drainage flows develop and persist with some consistency. However, during Episode 1 there is a mixing of warm air downwards into some, but not all, valleys. This occurs despite ambient winds remaining relatively low (generally around 3 m s^{-1}) and no evidence of cloud or fog; the two key meteorological conditions that control CAP and drainage flow formation (Sheridan *et al.*, 2014; Jemmett-Smith *et al.*, 2018). Episode 1 is characterised by intermittent increases and decreases in vertical velocities over a 1 h period near hill top height, which bookend a more sustained period of descent that occurs throughout the lidar profile depth at 23:00 UTC. Variations in radiosonde ascent rate and valley Ri_B calculations suggest this may be caused by wave activity leading to mixing, which occurs within a residual layer at and above hill top height. The exact cause of the wave activity during Episode 1 is not determined; however changes in wind direction at this time might lead to forcing of waves over the valley, and the profiles are conducive to the trapping of short wavelength waves. Changes in the valley ELR suggest the wave activity was not significant enough to break up the CAP and only temporary disruption of the drainage flows at Burfield and Duffryn is seen. The wave activity does not affect the entire Clun Valley region, at least not for a significant length of time, and the lowest areas with strong

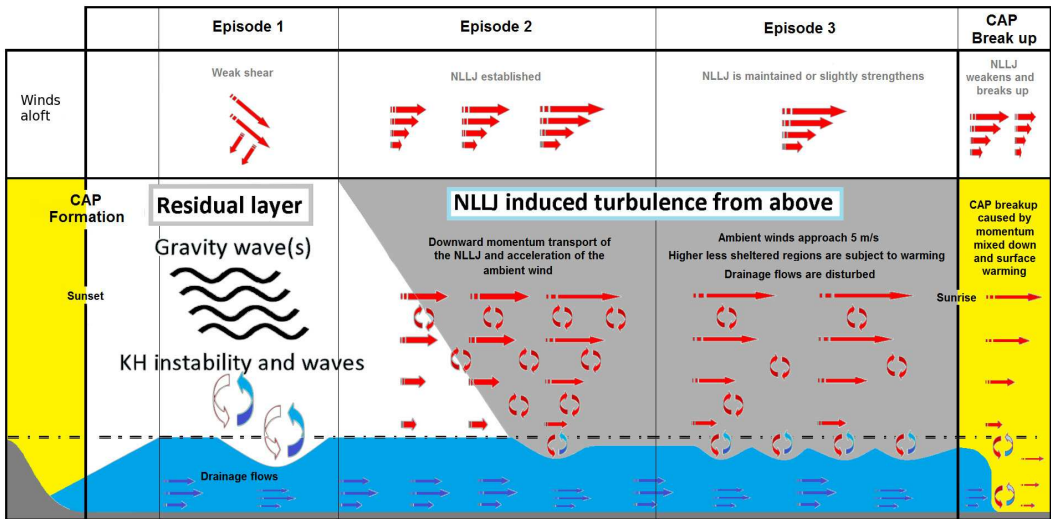


FIGURE 11 Illustration showing the sequence of events that cause CAP disruption during IOP 16. The yellow denotes daytime convective air, white is the residual layer, grey is air from aloft mixing into the residual layer and blue is the cold pool air in the valley.

near-surface stability are largely unaffected. For comparison, Adler *et al.* (2012) hypothesised local hydraulic jumps were the cause of episodic intrusions of warm air (up to 5 K warmer) into Arizona's Meteor Crater on clear, synoptically undisturbed nights; the CAP was not completely eroded and the lowest 30 m remained undisturbed. Whiteman *et al.* (2018a,b) provide evidence of these hydraulic jumps using dual Doppler lidar measurements. The study of Adler and Kalthoff (2016) also showed evidence of trapped waves / hydraulic jump leading to strong vertical velocities and mixing over a valley.

Episode 2 is characterised by a region of increased vertical velocity that descends over a 1.5 h period and coincides with an acceleration in the ambient wind in the residual layer (the formation of the NLLJ). By ~02:00 UTC the ambient winds stop accelerating and the region of increased vertical velocities dissipates. This feature is expected to signify the arrival of the NLLJ at hill top level as momentum is mixed down from above and the residual layer is completely eroded. An additional factor is likely to be the small increase in the geostrophic wind speed over the night and a slight change of direction as calculated from the operational surface pressure charts (e.g. Figure 2), although the radiosonde wind profiles suggest this occurs early on in the night.

The lidar vertical velocities throughout Episode 3 are larger in magnitude and are more turbulent in character. During Episode 3 the NLLJ continues to develop slowly, maintaining elevated winds near hill top level, close to thresholds found by others to initiate drainage flow and CAP breakup (Barr *et al.*, 1989; Orgill *et al.*, 1992; Bogren *et al.*, 2000; Iijima *et al.*, 2000; Whiteman *et al.*, 2001; Vosper and Brown, 2008). CAP breakup does not occur and drainage flows continue, but with some intermittent variations in wind speeds and screen temperatures, most notable in shallow valleys such as Burfield. CAP breakup occurs approximately 3 h after local sunrise at ~10:00 UTC – although some of the lowest sites remain cooler until ~10:35 UTC – and breakup is finally achieved when mixing-down of momentum from above occurs. Initial investigations of other IOPs during COLPEX suggest that NLLJs regularly occur during CAP nights. The exact role of the NLLJ in the timing of CAP breakup is an interesting question, given that the synoptic conditions for NLLJ and cold pool formation are similar, so that NLLJ influence is likely to be a fairly ubiquitous aspect of cold pool evolution.

Modelling CAP formation and evolution is a challenge, due to the small local scale of many of the dominant processes (small-scale orography leading to localised differences in surface energy balance, cooling and local drainage flows) and the difficulties of parametrising vertical mixing in stable boundary layers; however, other research as part of COLPEX suggests that at least in clear sky cases these processes are captured in very high resolution models (Vosper *et al.*, 2013, 2014; Hughes *et al.*, 2015). While NLLJs should be accurately modelled in simulations with sufficiently high resolution, other processes that lead/contribute to disruption of CAP evolution are a challenge. In particular, the wave activity observed during Episode 1 was not present in the simulations of Vosper *et al.* (2014). It is not clear whether this is due to differences in the temperature or wind profiles over the region preventing local generation of KH instability and/or gravity waves, or whether the disturbance was a feature propagating from outside the model domain. This is not an isolated case however, and Vosper *et al.* (2018) show data from another COLPEX IOP in which wave activity appeared to modulate near-surface temperatures and sensible heat fluxes in the Clun valley. The list of processes highlighted in this case study are not exhaustive and there are likely other SBL phenomena that influence CAP evolution with similar effect. More fundamentally, accurately modelling turbulence and the intermittent nature of SBLs remains a big challenge for numerical models (Holtslag *et al.*, 2013; Mahrt, 2014) and in recent times our understanding of the convective boundary layer has far outpaced that of the stable boundary layer (Fernando and Weil, 2010). Detailed observational case studies such as this are necessary to ensure the important physical processes at work in CAP evolution are documented, understood and are used to challenge the models in order to develop better representation of SBL processes in future.

5 | ACKNOWLEDGEMENTS

Bradley Jemmett-Smith was funded in this work through a UK Natural Environmental Research Council (NERC) Collaborative Award in Science and Engineering (CASE) studentship in collaboration with the UK Met Office. John Hughes' contribution was funded by the NERC and UK Met Office through the Joint Weather and Climate Research Programme under grant NE/I007679/1. The National Centre for Atmospheric Science (NCAS) provide financial support for the deployment of the lidar and AWS. The authors would like to thank all those involved in COLPEX, and in particular the Met Office Research Unit at Cardington who coordinated the field campaign. We would also like to thank the anonymous reviewers whose detailed comments substantially improved this manuscript.

REFERENCES

- Adler B, Whiteman CD, Hoch SW, Lehner M, Kalthoff N. 2012. Warm-Air Intrusions in Arizona's Meteor Crater. *J. Appl. Meteorol. Climatol.*, **51**, 1010–1025.
- Adler B, Kalthoff N. 2016. The impact of upstream flow on the atmospheric boundary layer in a valley on a mountainous island. *Boundary-Layer Meteorol.*, **158**, 429–452.
- Banta RM, Darby LS, Fast JD, Pinto JO, Whiteman CD, Shaw WJ, Orr BW. 2004. Nocturnal low-level jet in a mountain basin complex. Part I: Evolution and effects on local flows. *J. Appl. Meteorol.*, **43**, 1348–1365.
- Barr S, Orgill MM. 1989. Influence of external meteorology on nocturnal valley drainage winds. *J. Appl. Meteorol.*, **28**, 497–517.
- Bogren J, Gustavsson T, Postgård U. 2000. Local temperature differences in relation to weather parameters. *Int. J. Climatol.*, **20**, 151–170.
- Clements CB, Whiteman CD, Horel JD. 2003. Cold-air-pool structure and evolution in a mountain basin: Peter Sinks, Utah. *J. Appl. Meteorol.*, **42**, 752–768.

- Coulter RL, Orgill M, Porch W. 1989. Tributary fluxes in to Bruch Creek Valley. *J. Appl. Meteorol.*, **28**, 555–568.
- Daly C, Conklin DR, Unsworth MH. 2010. Local atmospheric decoupling in complex topography alters climate change impacts. *Int. J. Climatol.*, **30**, 1857–1864.
- Fernando HJS, Weil JC. 2010. Whither the stable boundary layer? A shift in the research agenda. *Bull. Am. Meteorol. Soc.*, **91**, 1475–1484.
- Gudiksen PH, Leone JM, King CW, Ruffieux D, Neff WD. 1992. Measurements and modelling of the effects of ambient meteorology on nocturnal drainage flows. *J. Appl. Meteorol.*, **31**, 1023–1032.
- Gustavsson T, Karlsson M, Bogren J, Lindqvist S. 1998. Development of temperature patterns during clear nights. *J. Appl. Meteorol.*, **37**, 559–571.
- Heywood GSP. 1933. Katabatic winds in a valley. *Quart. J. Roy. Meteorol. Soc.*, **59**, 47–58.
- Holtslag AAM, Svensson G, Baas P, Basu S, Beare B, Beljaars ACM, Bosveld FC, Cuxart J, Lindvall J, Steeneveld GJ, Tjernström M. 2013. Stable atmospheric boundary layers and diurnal cycles: challenges for weather and climate models. *Bull. Am. Meteorol. Soc.*, **94**, 1691–1706.
- Hughes JK, Ross AN, Vosper SB, Lock AP, Jemmett-Smith BC. 2015. Assessment of valley cold pools and clouds in a very high resolution NWP model. *Geosci. Model Dev.*, **8**, 4453–4486.
- Iijima Y, Shinoda M. 2000. Seasonal changes in the cold-air pool formation in a subalpine hollow, central Japan. *Int. J. Climatol.*, **20**, 1471–1483.
- Jemmett-Smith BC, Ross AN, Sheridan PF. 2018. A short climatological study of cold air pools and drainage flows in small valleys. *Weather*, **73**, 256–262.
- Lareau NP, Crosman E, Whiteman CD, Horel JD, Hoch SW, Brown WOJ, Horst TW. 2013. The persistent cold-air pool study. *Bull. Am. Meteorol. Soc.*, **94**, 51–63.
- Lareau NP, Horel JD. 2015. Turbulent Erosion of Persistent Cold-Air Pools: Numerical Simulations. *J. Atmos. Sci.*, **72**, 1409–1427.
- Largeroy Y, Staquet C, Chemel C. 2013. Characterization of oscillatory motions in the stable atmosphere of a deep valley. *Boundary-Layer Meteorol.*, **148**, 439–454.
- Lindkvist L, Gustavsson T, Bogren J. 2000. A frost assessment method for mountainous areas. *Agri. Forest Meteorol.*, **102**, 51–67.
- Madelin M, Beltrando G. 2005. Spatial interpolation-based mapping of the spring frost hazard in the Champagne vineyards. *Meteorol. App.*, **12**, 51–56.
- Mahrt L, Richardson S, Seaman N, Stauffer D. 2010. Non-stationary drainage flows and motions in the cold pool. *Tellus A.*, **62**, 698–705.
- Mahrt L. 2014. Stably stratified atmospheric boundary layers. *Ann. Rev. Fluid Mech.*, **46**, 23–45.
- Mahrt L, Heald R. 2015. Common marginal cold pools. *J. Appl. Meteorol. Climatol.*, **54**, 339–351.
- Manins PC, Sawford BL. 1979. Katabatic winds: A field case study. *Quart. J. Roy. Meteorol. Soc.*, **105**, 1011–1025.
- Orgill MM, Kincheloe JD, Sutherland RA. 1992. Mesoscale influences on nocturnal valley drainage winds in Western Colorado valleys. *J. Appl. Meteorol.*, **31**, 121–141.
- Pozdnoukhov A, Foresti L, Kanevski M. 2009. Data-driven topo-climatic mapping with machine learning methods. *Nat. Hazards*, **50**, 497–518.

- Price JD, Vosper S, Brown A, Ross AN, Clark P, Davies F, Horlacher V, Claxton B, McGregor JR, Hoare JS, Jemmett-Smith B, Sheridan P. 2011. COLPEX: Field and Numerical Studies Over a Region of Small Hills. *Bull. Am. Meteorol. Soc.*, **92**, 1636–1650.
- Renfrew IA. 2004. The dynamics of idealized katabatic flow over a moderate slope and ice shelf. *Quart. J. Roy. Meteorol. Soc.*, **130**, 1023–1045.
- Sheridan PF, Vosper SB, Brown AR. 2014. Characteristics of cold pools observed in narrow valleys and dependence on external conditions. *Quart. J. Roy. Meteorol. Soc.*, **140**, 715–728.
- Sheridan PF, Vosper SB, Smith SA. 2018. A physically-based algorithm for downscaling temperature in complex terrain. *J. Appl. Meteorol. Climatol.*, **57**, 1907–1929.
- Stull RB. 1988. *An Introduction to Boundary Layer Meteorology*. Kluwer Academic Publishers.
- Thorpe AJ, Guymer TH. 1977. The nocturnal jet. *Quart. J. Roy. Meteorol. Soc.*, **103**, 633–653.
- Vosper SB, Brown AR. 2008. Numerical simulations of sheltering in valleys: The formation of nighttime cold-air pools. *Boundary-Layer Meteorol.*, **127**, 429–448.
- Vosper SB, Carter E, Lean H, Lock A, Clark P, Webster S. 2013. High resolution modelling of valley cold pools. *Atmos. Sci. Lett.*, **14**, 193–199.
- Vosper S, Hughes JK, Lock AP, Sheridan PF, Ross AN, Jemmett-Smith B, Brown AR. 2014. Cold pool formation in a narrow valley. *Quart. J. Roy. Meteorol. Soc.*, **140**, 699–714.
- Vosper SB, Ross AN, Renfrew IA, Sheridan PF, Elvidge AD, Grubišić V. 2018. Current challenges in orographic flow dynamics: turbulent exchange due to low-level gravity-wave processes. *Atmosphere*, **9**, 361.
- Whiteman CD, Doran JC. 1993. The relationship between overlying synoptic-scale flows and winds within a valley. *J. Appl. Meteorol.*, **32**, 1669–1682.
- Whiteman CD, Zhong S, Shaw WJ, Hubbe JM, Bian X, Mittelstadt J. 2001. Cold pools in the Columbia Basin. *Wea. Forecasting.*, **16**, 432–447.
- Whiteman CD, Lehner M, Hoch SW, Adler B, Kalthoff N, Haiden T. 2018. Katabatically driven cold air intrusions into a basin atmosphere. *J. Appl. Meteorol. Climatol.*, **57**, 435–455.
- Whiteman CD, Lehner M, Hoch SW, Adler B, Kalthoff N, Vogt R, Feigenwinter I, Haiden T. Hills MOG. 2018. The nocturnal evolution of atmospheric structure in a basin as a larger-Scale katabatic flow is lifted over its rim. *J. Appl. Meteorol. Climatol.*, **57**, 969–989.
- Zängl, G. 2008. Dynamical aspects of wintertime cold-air pools in an Alpine valley system. *Mon. Wea. Rev.*, **133**, 2721–2740.